A comparison of Space Weather analysis techniques used to predict the arrival of the Earth-directed CME and its shockwave launched on 8 April 2010

C. J. Davis[1], C. A. de Koning[2], J. A. Davies[1], D. Biesecker[2], G. Millward[2], M. Dryer[2], C. Deehr[3], D. F. Webb[4], K. Schenk[5], S. L. Freeland[6], C. Möstl[7], C. J. Farrugia[8], D. Odstrcil[9]

[1] STFC Rutherford Appleton Laboratory, Chilton, Oxfordshire, UK

[2]NOAA/SWPC, Boulder Colorado, USA

[3]GI Univ. of Alaska, Fairbanks, USA

[4]ISR, Boston College, Chestnut Hill, MA, USA

[5]NASA-Goddard Space Flight Center, USA

[6]Lockheed Martin Solar and Astrophysics Laboratory

[7]Space Research Institute, Austrian Academy of Sciences, Schmiedlstr, Graz, Austria

[8]University of New Hampshire, USA

[9]University of Colorado at Boulder, USA

Abstract

The Earth-directed Coronal Mass Ejection (CME) of 8 April 2010 provided an opportunity for space-weather predictions from both established and developmental techniques to be made from near-real time data received from the SOHO and STEREO spacecraft; the STEREO spacecraft provide a unique view of Earth-directed events from outside the Sun-Earth line. Although the near-real time data transmitted by the STEREO Space Weather Beacon are significantly poorer in quality than the subsequently down-linked science data, the use of these data has the advantage that near-real time analysis is possible, allowing actual forecasts to be made. The fact that such forecasts cannot be biased by any prior knowledge of the actual arrival time at Earth provides an opportunity for an unbiased comparison between several established and developmental forecasting techniques. We conclude that for forecasts based on the STEREO coronagraph data, it is important to take account of the subsequent acceleration/deceleration of each CME through interaction with the solar wind, while predictions based on measurements of CMEs made by the STEREO Heliospheric Imagers would benefit from higher temporal and spatial resolution. Space weather forecasting tools must work with near-real time data; such data, when provided by science missions, is usually highly compressed and/or reduced in temporal/spatial resolution and may also have significant gaps in coverage, making such forecasts more challenging.

Introduction

An Earth-directed Coronal Mass Ejection (CME) was launched on 8 April 2010. This CME provided an excellent opportunity for the comparison of space-weather predictions, from both well established and developmental techniques, to be made using the near-real time data received from SOHO (Fleck, Domingo and Poland, 1995) and STEREO (Russell, 2008). For SOHO, CME characteristics were determined from the LASCO C2 and C3 coronagraphs (with fields of view from 1.5-6 R_{sun} and 3.8-32 R_{sun} respectively) (Brueckner et al., 1995). For STEREO, data from the SECCHI (Sun Earth Connection Coronal and Heliospheric Investigation) suite of instruments (Howard et al., 2008) were used. SECCHI comprises five telescopes, which together image the solar corona from the solar disk to beyond 1 AU. These telescopes are: an extreme ultraviolet imager (EUVI: 1—1.7R_{sun}), two traditional Lyot coronagraphs (COR1: 1.5-4R_{sun} and COR2: 2.5-15R_{sun}), and two Heliospheric Imagers (HI-1: 15-84R_{sun} or 4^{o}-24^{o} elongation and HI-2: 66-318R_{sun} or 18^{o}-88^{o} elongation). Detailed observations of this event were also made by the Solar Dynamic Observatory but these were not used in the near real-time forecasts described in this paper.

A CME observed in the interplanetary medium is often referred to as an Interplanetary CME or ICME. While the terms CME and ICME are often used when referring to the same event, the distinction can be useful since a CME (usually observed in coronagraph data) may have undergone some evolution in structure by the time it is observed in the interplanetary medium. Likewise, a subset of ICMEs is referred to as magnetic clouds (MCs). These are characterized as having an enhanced magnetic field, a magnetic field vector that rotates through a large angle, a low proton temperature and a low plasma β (a measure of the plasma pressure normalized to the magnetic field strength). While the event in this study is, in general, referred to here as a CME, the terms ICME and MC are used when referring to the event at later times in its evolution.

The near-real time data transmitted by the STEREO Space Weather Beacon (Biesecker et al., 2008) are significantly degraded compared with the subsequently down-linked science data, and contain more gaps due to the challenges of receiving a continuous data stream from such distant spacecraft. While the beacon data are lower in both spatial and temporal resolution, and more highly compressed, using these near-real time data has the advantage of allowing actual forecasts to be made. The fact that such forecasts cannot be biased by any prior knowledge of the actual arrival time at Earth (as determined for example with in-situ instrumentation), provides an opportunity for an unbiased comparison of forecasting techniques. This paper outlines several of these techniques and compares the forecasts made by each of them in advance of the arrival at Earth of the 8 April CME.

Observations

Five predictions were made of the arrival time of this CME and its shock at Earth, using a variety of methods. STEREO coronagraph data (Howard et al., 2008) were used to estimate the speed and direction of the CME, as were data from the STEREO Heliospheric Imagers (Eyles et al., 2009). Another prediction was made from the STEREO coronagraph data but with the application of a correction for any modulation of the CME speed by the ambient solar wind. Furthermore, STEREO and SOHO coronagraph data were used as inputs to two separate runs of the Enlil Heliospheric model (Odstrcil and Pizzo, 1999a,b). A separate prediction of the CME’s shockwave arrival at Earth was made with the Shock Time of Arrival model (STOA, Dryer and Smart, 1984) based on classical blast wave theory (Sedov, 1959). These techniques are discussed in more detail in the following sections and their predictions are summarized in Tables I and II.

A B3.7 long duration flare occurred in NOAA Active Region 11060 at N25°E16° (as viewed from Earth) starting on 8 April at 02:30 UT. It was associated with an erupting filament, a coronal wave and double dimming areas as observed in EUV. The surface event was observed with both STEREO-A (on the northeast limb) and STEREO-B (just on the northwest disk) with initial activity at 02:40. A later eruptive prominence on the solar limb (EPL) was noted in EUVI images from STEREO-A (EUVI-A) at 304 Å starting at 04:06 from the same northeast region. At the time of these observations, STEREO-A was positioned 84.4^{o} longitude ahead of the Earth and STEREO-B was positioned 82.6^{o} longitude behind the Earth (in Heliocentric Earth Ecliptic, HEE, coordinates).

The SOHO/LASCO C2 coronagraph observed a bright CME rising over the northeast limb (Position Angle, PA, ~70°) at 03:30 followed by a ragged front over the southwest limb (PA ~245°) starting at 04:30. The event quickly developed into a full halo that was first seen in LASCO C3 images starting at 06:18. A speed of 286 kms^{-1} at PA 240° was determined from the LASCO data (see EIT and LASCO data at: http://umbra.nascom.nasa.gov/lasco/observations/halo/100408/). The STEREO/COR instruments observed a relatively typical yet bright CME with a width of 50 to 60°. The COR1 instruments on both STEREO spacecraft first observed material associated with this CME at 03:15 and COR2-A first observed it at 04:08. Considering all the SOHO and STEREO observations, it seems that the two bright structures that were separated by nearly 180° in LASCO were part of the single halo event directed Earthward.

Properties of the source region on the Sun were also discussed prior to the arrival of the ICME at Earth, with respect to forecasting the orientation and handedness of the possible resulting magnetic cloud (MC). The orientation of the MC is linked to the length and strength of the southward ($–B_z$) magnetic field interval at Earth (e.g. Zhao and Hoeksema, 1998).

Figure 1 shows a collage of images which were used in real time to determine several parameters which have been found to influence the orientation of the MC (see, for example, the summary in Yurchyshyn et al., 2001). For the sake of simplicity, we just discuss the orientation and not the detailed structure of the source region (for example, the possible MC chirality and axial field direction), because later at Earth an ICME with no clear internal magnetic field rotation was observed (see below). In figure 1a, the active region neutral line lies along a northwest – southeast axis, tilted by approximately 40^{o} to the solar equator when measured to the solar west. Figure 1b shows the coronal neutral line (GONG PFSS model, http://gong.nso.edu) being approximately perpendicular to the active region neutral line with an inclination of approximately -50^{o}. In figure 1c, it is seen that the halo CME observed by LASCO (http://lasco-www.nrl.navy.mil/daily_mpg/) was between these two extremes, with an inclination of around -20^{o}. With such a wide variety of orientations, it was not straightforward to predict the orientation of the resulting magnetic cloud associated with the CME. However, the point is that the tilt of the coronal neutral line made it likely that the magnetic cloud would also be tilted with respect to the solar equator or the ecliptic (Yurchyshyn, 2008), and it was therefore possible that the CME, if Earth directed, would produce a reasonably sustained period of negative Bz and a small geomagnetic disturbance.

At L1 a shock was detected by both the ACE (Stone et al., 1998) and WIND spacecraft (Ogilvie and Parks, 1996). While the WIND spacecraft has not always been positioned at L1, it was at the time of these observations. Data from the SWEPAM instrument (McComas et al., 1998) onboard the ACE spacecraft showed the arrival of an ICME shock front at 12:14 on 11 April (indicated by the vertical line in figure 2). The passage of the ICME can be inferred from an increase in solar wind proton number density from 2 to 8 cm^{-3} accompanied by a rotation of the magnetic field vector and an increase in magnetic field strength indicating a possible magnetic cloud. Over the same time interval, the solar wind bulk speed increased from approximately 380 kms^{-1} to 450 kms^{-1}. Using the latter as an indicator of the ICME speed suggests that the shock arrival time at Earth would be almost exactly an hour later than at ACE. The geomagnetic field underwent a sudden impulse at 13:05 on the same day caused by the arrival of the shock at Earth. The accompanying southward field resulted in a small geomagnetic storm; Kp reached 6 and DsT -66 nT early on 12 April.

Plasma and magnetic field observations from the SWE (Ogilvie et al., 1995) and the MFI (Lepping et al., 1995) instruments on Wind are shown in Figure 3 for the time interval 12 UT, 10 April to 12 UT, 13 April. The data are at ~95 s temporal resolution. From top to bottom are plotted the proton number density, temperature, bulk speed, dynamic pressure, total field strength and components of the magnetic field in GSE coordinates, the proton beta (in red: the Alfven Mach number) and the pressures (red: magnetic; blue: proton thermal; black: their sum). The red trace in panel 2 is the expected proton temperature for normal solar wind expansion after the statistical analysis of Lopez (1987).

The shock is denoted by 'S' at the first vertical line in figure 3. The interval 22 UT, 11 April, to 14 UT, 12 April, bracketed by the second and third vertical guidelines, is characterized by signatures of an ICME: (i) low proton temperature (compared with the expected ones) and beta (Gosling et al., 1973; Richardson and Cane, 1995; (ii) higher-than-average magnetic field strengths; and (iii) low Alfven Mach numbers (average = 5.3) (Farrugia et al., 1995;

Lavraud and Borovsky, 2008). A large and smooth rotation of the magnetic field is absent, so this structure is not likely to be a magnetic cloud with a typical flux rope structure.

Thus the orientation of the resulting ICME could not be determined nor related to the orientation parameters close to the Sun as discussed above. It is interesting to note that the sheath region behind the shock of the ICME was mainly responsible for the long negative B_z interval leading to the geomagnetic storm, a relationship that has been discussed by previous authors (e.g. Gosling and McComas, 1987).

Figure 4 shows the pitch angle distribution of suprathermal electrons (Ogilvie et al., 1971; Pilipp et al., 1987) centered on E = 193.4 eV during the ICME interval. The data are from the SWE/electron instrument and are plotted at 12 s resolution. It is seen that the strahl electrons, which carry the heat flux from the Sun, are generally unidirectional: Electrons are flowing against the field (large PA) until ~1 UT, 12 April, and then are flowing along the field (small PA). Inspection of the B_x component of the magnetic field (positive towards the Sun), reveals a switch from positive to negative B_x at around 1 UT, indicating that these electrons are flowing out from the Sun throughout this period. Thus we may conclude that the "feet" of the field lines are connected to the Sun at only one end. There is, however, a brief interval centered on 4 UT, 12 April, when the electrons are omnidirectional located in the ICME front part.

Data used in the forecasts

The data used in the various forecasting techniques came from the two solar missions, SOHO and STEREO, and the operational satellite from the NOAA Geostationary Operational Environment Satellite (GOES) program.

The STEREO/SECCHI data used in the predictions were transmitted by the STEREO Space Weather Beacon, which is a continuous, real-time, low data-rate (633 bps) broadcast of the data from STEREO. The current allocation for the SECCHI space weather data is 500 bits/s (Biesecker et al., 2008) but this allocation will continue to be reduced due to telemetry constrains as the mission evolves. Since the full STEREO data set cannot be down-linked in the beacon, this low data rate requires careful choices of the data to be transmitted. In concert with the instrument teams, a scheme has been devised to ensure that the resulting data will retain its value to space weather forecasters. In particular, COR2 images are compressed using ICER, a lossy wavelet image compression scheme, and binned down from their original size of 2048x2048 pixels to 256x256 pixels. The images from the inner HI-1 cameras are binned down to 256x256 pixels and lossily compressed. The central 16 bits from each 32 bit HI-2 image are transmitted via the beacon after being cropped from the nominal 1024x1024 to a subfield of 512x1024 (the sunward half) and losslessly compressed. Although the beacon data are noisier than the science-quality data, the combined compression and binning schemes provide sufficient signal-to-noise for denser-than-ambient structures such as CMEs to be imaged. Thus, they can be used for space weather forecasting. The COR2 beacon data are transmitted every 15 min, whereas the HI-1 and HI-2 data are transmitted every 2 hours; note that the number of images actually received depends on one or more antennas being available to track the STEREO spacecraft at that time, unlike the science data for which there is a dedicated daily down-link scheduled. Apart from these changes, SECCHI images from the space weather beacon undergo the exact same on-board processing and ground processing, at the STEREO Science Center (Eichstedt et al., 2008), as the science-quality images.

Coronagraph geometric/polarization localization results

STEREO COR2, rather than COR1, data were used to analyze CME propagation near the Sun, since the much larger COR2 field-of-view allows the evolution of a CME to be observed, thus allowing its velocity to be calculated, even for very fast CMEs. Examples of COR2 beacon percent polarization and science total brightness images from STEREO-A and STEREO B are presented in figure 5. Within the COR2 field-of-view, CME propagation was analyzed using geometric and/or polarimetric localization. The geometric localization technique (Pizzo and Biesecker, 2004; de Koning et al., 2009; de Koning and Pizzo, 2010) uses a series of lines-of-sight from two space-based coronagraphs to determine gross propagation characteristics of CMEs in three-dimensional space. The polarimetric localization technique [Moran and Davila, 2004; de Koning and Pizzo, 2010] uses the percentage polarization observed by a single coronagraph to obtain a three-dimensional reconstruction of a CME. Both of these techniques readily provide an initial estimate of the CME speed and direction of propagation.

Both techniques were used in real-time to predict the speed and direction of propagation of the 8 April 2010 CME. The CME entered the COR2-A field-of-view at 04:00 and started to exit COR2-A at 08:00. Similarly, the CME density front entered the COR2-B field-of-view at 04:30 and started to exit COR2-B at 08:00. In near-real time, the total brightness image and polarization sequence for 05:09 were missing from STEREO-A, and the total brightness image from 07:39 was missing from STEREO-B. For convenience, we decided to use an identical data set for both techniques since this did make it easier to directly compare outcomes. The only times that polarization data were simultaneously available from both spacecraft, while the CME was in the COR2 field of view, were at 06:09, 07:09 and 08:09. Applying either geometric or polarimetric localization to the images at these three times resulted in plots of 3D position vs time, from which the CME velocity was calculated. The techniques were used to calculate both the centroid and leading-edge velocity of the CME. As described by de Koning et al., [2009] and de Koning and Pizzo [2010], the velocity calculation for each technique was repeated five times, to account for uncertainties introduced by using hand drawn boundaries to identify the CME in the COR2 field of view. An example of the reconstructed CME is shown in figure 6; the view is for an observer looking down onto the north pole of the Sun. The cluster of red points is the CME location derived from COR2-A percent polarization measurements, the cluster of blue points is the

CME location derived from COR2-B percent polarization measurements, while the quadrilaterals of the CME as a whole, obtained from geometric localization, are shown in green; superimposed on this stack are purple quadrilaterals showing the location of the CME leading edge.

Three predicted CME speeds and directions of propagation were reported on 9 April at 04:51 to an email distribution list associated with the STEREO mission that reaches a worldwide audience of interested scientists. This prediction and subsequent emails were made available via the STEREO Space Weather Group website (http://secchi.nrl.navy.mil/spwx/). The three predictions were based on geometric localization, and polarimetric localization applied to STEREO-A and -B separately. The reported results consisted of the average leading-edge speed obtained from the five runs, and the average centroid longitude and latitude of propagation. The reported error in each quantity was one standard deviation calculated from the five runs. We used the centroid direction of propagation, instead of the leading-edge direction, since we assume that the direction of CME propagation will be mostly determined by its bulk characteristics. All results below are in Heliocentric-Earth-Equatorial (HEEQ) coordinates.

Using the geometric localization technique, we found that while the CME was in the COR2 field of view, it had a leading edge speed of 469 ± 27 kms^{-1} and a direction of propagation of $2^o \pm 13^o$ east and $6^o \pm 3^o$ north. Using the COR2 polarisation data from STEREO-A, we found a leading-edge speed of 473 ± 59 kms^{-1} and a direction of propagation of $11^o \pm 3^o$ west and $7^o \pm 3^o$ south. Using the COR2 polarisation data from STEREO-B, we found a leading-edge speed of 545 ± 42 kms^{-1} and a direction of propagation of $15^o \pm 1^o$ east and $8^o \pm 2^o$ south.

Considering that the results obtained from the polarimetric localization technique are biased to the spacecraft's plane of sky, we averaged the longitude obtained from STEREO-A and STEREO-B resulting in a direction of 2^o east, identical to the result obtained from geometric localization, with an average estimated speed of 509 ± 72 kms^{-1}.

As noted above, the predicted CME velocities were based on a minimal data set of only three time steps available from the real-time beacon data. In order to ascertain whether the prediction made using these techniques was limited by the input data, the same analyses were applied to the higher resolution science data that became available after the event. The primary advantage to applying geometric localization to science data is the increase in data points, from 3 to 12. This retrospective analysis resulted in a leading-edge speed of 530 ± 30 kms^{-1} and a direction of propagation of $2^o \pm 7^o$ east and $11^o \pm 7^o$ south. In the case of polarimetric localization, the use of the science data resulted in only a slight change in the number of data points, from 3 to 4. Because the polarimetric localization technique returns only the gross CME characteristics, using higher spatial resolution data did not perceptibly alter the results with such a small change in the number of data points.

As the CME develops, additional techniques could be used to update the forecast. For very slow CMEs, science quality data may even be used to further improve the forecast. However, this option is not available for the fastest, and thus most geo-effective, CMEs.

STEREO Heliospheric Imager technique and results

As part of the SECCHI suite of instruments, each of the twin STEREO spacecraft carries a Heliospheric Imager (HI). These instruments each contain two visible-light wide-field cameras that are capable of tracking plasma density fronts associated with CMEs by detection of sunlight that has undergone Thomson-scattering within the plasma. Sheeley et al. (1999) suggested that the speed and direction of solar wind transients such as CMEs could be estimated from the apparent acceleration in the elongation variation for transients viewed out to large elongations. Such analysis assumes that the transient propagates at a constant speed in a fixed direction. Such analysis of STEREO HI data (Sheeley et al., 2008, Rouillard et al., 2008, Davis et al., 2009) has demonstrated that this technique is applicable to solar transients such as CMEs propagating within the HI field of view and that the estimated arrival times at various locations in the heliosphere can be ratified by in-situ observations. Subsequently, Davis et al. (2010) carried out a survey in which they compared the speed and direction of ICMEs determined from the HI data using this technique with CME values estimated from a forward modeling technique based on STEREO coronagraph data (Therniesien et al., 2010). Their work showed good agreement between the two techniques in terms of the estimated CME propagation direction but revealed a systematic difference between the speed of CMEs measured in the coronagraphs and in HI. This difference was dependent on the speed of each CME, with faster CMEs tending to be decelerated and slower CMEs being accelerated between the two fields of view. The authors surmised that this was due to interaction with the ambient solar wind. Comparison with in-situ observations for two of the events within this survey resulted in the predicted arrival of each CME matching in-situ observations within five or six hours. While the assumption of a fixed (average) speed of CME propagation leads, in general, to accurate predicted arrival times at 1 AU, these average speeds are often markedly different from the solar wind speeds that are measured in-situ. This is further evidence that some modification of the CME speed can occur, as discussed by previous authors (e.g. Gopalswamy et al., 2000; Jones et al. 2007).

The validation of the above technique was carried out retrospectively using the higher-resolution science data. Examples of both science and beacon images from the HI-1 cameras on STEREO-A and STEREO-B are presented in figure 7.

For the CME launched on 8 April 2010, plots of elongation versus time at a fixed PA, so-called J-maps (e.g. Davies et al., 2009), were produced from the HI-1 and 2 images received in the STEREO space-weather beacon (figures 8a and 8b). As the J-map from the Ahead spacecraft contained a large data gap, the analysis was carried out on the data from STEREO-B since this was more complete. The time/elongation profile, extracted from the HI-B J-map, was analyzed on 9 April 2010 using the method described above, to fit a speed and direction to the 8 April CME. The leading edge of the feature was identified and manually scaled five times in order to characterize the level of uncertainty introduced by the manual scaling. From this analysis the ICME was predicted to be propagating at a speed of 417 ± 67 kms^{-1} at a solar longitude (in HEE coordinates) of $12^o \pm 17^o$ East (i.e. behind the Earth in its orbit). This gave an estimated arrival time at Earth of 00:27 on 12 April (±2.5 hours). A subsequent analysis, carried out on 10 April (when more beacon data had been collected) refined this estimate to 410 ± 67 kms^{-1} propagating along a solar longitude of $-3^o \pm 14^o$ East and a predicted arrival time at Earth of 02:13 UT on 12 April (± 1.3 hours).

When the analysis was repeated after the event using the HI science data (figures 8c and 8d), the same technique estimated the ICME front to be travelling at a speed of 482 ± 15 kms^{-1} along a solar longitude of $11.7^o \pm 4^o$ East (behind Earth), giving an estimated arrival time at Earth of 14:40 on 11 April (± 2 hours). This result was robust even when the science data were restricted to the elongation range used in the predictions from the beacon data (although the uncertainty increased slightly). It is clear that, on this occasion at least, this technique would have benefitted from beacon data that were of higher spatial and temporal resolution. Reducing the resolution may introduce a small systematic error for a given event since the actual position of the CME within each binned pixel is unknown. The sign of such systematic errors would be random between different events. Such systematic errors would affect the fitting process but the exact influence would depend on the speed and direction of each CME. It is also apparent that the uncertainties quoted for the current prediction are far smaller than the uncertainties introduced by the lower temporal and spatial resolution of the beacon data. More work must be done to characterize the uncertainties introduced by the reduced resolution of the beacon data.

If the angle of propagation of an ICME can be estimated from an independent technique, this parameter can be fixed in the analysis of the HI data and a true time/height profile throughout the ICME propagation can be made. In this way, it becomes possible to assess the assumption that an ICME does not accelerate within the HI field of view provided the propagation direction remains fixed. Since the angle of propagation estimated from the coronagraph data and the HI data were similar for this event (and indeed, many of those events discussed in the survey by Davis et al., 2010) it seems reasonable to use the angle of propagation from the coronagraph data to derive the time/height profile from the HI observations. When this is done for the 8 April 2010 ICME the resulting time/height profile is linear (within the uncertainties of the measurements) so, for this event, no detectable acceleration occurs within the HI field of view.

'Biesecker' technique and results

Biesecker and colleagues used an empirical algorithm that uses the CME initial velocity, the solar wind speed, and the source location of the CME to predict the onset time of the sudden impulse (SI) at Earth. Whenever a SOHO/LASCO team halo CME alert indicates a front-sided halo or partial halo CME, the empirical algorithm is employed.

The definitions of halo and partial halo CMEs used by this alert system are discussed in detail elsewhere (St Cyr, 2005) but in summary, a halo CME is one in which the CME surrounds the coronagraph occulting disk with an apparent width of 360^o. Full halos can be either symmetric or asymmetric depending on the origin and position angle of the CME. Partial halo events are classified by those CMEs that have an apparent width of at least 180^o From the view of LASCO, along with data from the inner coronal instruments which provide proof of origin, a halo is classified as either front-sided (Earth directed) or back-sided (travelling away from the Earth).

The empirical algorithm discussed in this section was derived from looking at 31 well identified and isolated halo CMEs observed with SOHO/LASCO and using only parameters that would be easily available to forecasters. The algorithm first assumed a ballistic solution and then the developers found the onset time error could be minimized by accounting for acceleration/deceleration in the solar wind (assuming an aerodynamic drag equivalent force, $(V_{ACE}-V_{CME})^2$) and a cosine correction for the source location of the CME. Using the requirement that data had to be accessible to forecasters, the technique uses the CME speed reported by LASCO and uses the hourly averaged solar wind speed observed at ACE at the time the CME is first seen in LASCO C2. It was found that the uncertainty in arrival time at Earth for this technique depended on the speed of the CME. For CMEs with speeds of less than 500 kms^{-1}, the average uncertainty in arrival time was 7.2 hours, for CMEs travelling between 500 and 1000 kms^{-1} the average uncertainty was 9.7 hours and for the fastest CMEs (above 1000 kms^{-1}) the average uncertainty in arrival time was 5.7 hours. For the CME of 8 April 2010, this technique predicted an arrival time at Earth of 06:30 UT on 11 April ± 8 hours.

Currently the estimate of the background solar wind speed is made from measurements at the ACE spacecraft at the time of the CME launch. There is no guarantee that this speed is representative of the solar wind speed throughout the inner heliosphere during the propagation of the CME. Using a measure of the solar wind speed that better represents these conditions should improve the accuracy of this technique but initial attempts to refine the estimate of the ambient solar wind speed using predictions from the Wang-Sheeley-Arge (WSA) model (Arge et al., 2004) did not improve the uncertainty in arrival time when applied to the 31 events used to test this technique. The reason why the WSA model did not improve the predictions is, as yet, unclear but may have something to do with the reduced accuracy of the WSA during periods of high solar activity as was the case for most of the 31 test events.

Enlil technique and results

The Enlil model is a numerical MHD model of the heliosphere. It models a CME by launching a spherical, over-pressured, hydrodynamic plasma cloud into a steady-state background solar wind. From this it calculates parameters such as plasma density, velocity, temperature and magnetic field in 4D (space and time). It can therefore be used to make predictions of the arrival of the leading edge of the bulk ICME plasma cloud at Earth.

The basic driver for the model is a velocity field which is defined at the Enlil inner boundary of 21.5 R_{sun}. This velocity field is derived from the WSA model (Arge et al., 2004) which itself takes solar magnetograms, in this case from the National Solar Observatory Global Oscillation Network Group (GONG; Wing, 1998), and calculates this velocity field. So, by itself, WSA-Enlil produces a measure/prediction of the 'ambient' solar wind.

It is possible to introduce a proxy CME into this model and make predictions about its propagation. Within the model, a CME is defined as a sphere of enhanced plasma density that occurs at a given point on the inner boundary (i.e., latitude, longitude, time) and has a specified velocity and angular width.

The current version of Enlil can predict background magnetic field and the effects of the shock compression and magnetic field draping around ejecta but cannot predict the internal magnetic structure of transients. It traces the ejected (hydrodynamic) cloud which enables it to differentiate between four scenarios in geospace: no disturbance, shock, ejecta, shock plus ejecta.

For the event of 8 April 2010, the CME attributes were estimated in two ways, and the model was run twice, once for each set of input parameters. The first model run (ENLIL_1) used CME parameters derived from the STEREO/COR2 coronagraphs as described in the coronagraph analysis section above. The resulting prediction was for an ICME arriving at Earth at 09:00 on 11 April.

The second model run (ENLIL_2) used the elliptical cone method of Xie et al. (2004) to analyze SOHO/LASCO C3 coronagraph images. Using difference imaging it is possible to define a series of Sun-centered ellipses from which the essential CME parameters can be calculated. The prediction from this model run was for an ICME arriving at Earth at 21:00 on 11 April 2010.

The difference between the two Enlil predictions is largely due to the different inputs used in each model run. While the directions were similar in each case, the estimations of radial velocity used were 500 kms^{-1} and 378 kms^{-1} respectively. The difference in ICME event timings were just for the time at which the basic density pulse arrived at Earth. Note, in the Enlil model there is no distinction between Earth and L1 - both are the same grid point within the resolution of the model.

Shock Time of Arrival (STOA) technique and results

The STOA model was used to forecast the interplanetary shock wave's arrival using a modification and application of the classical blast wave model (Dryer and Smart, 1984; Smart and Shea, 1985; and Smith et al., 2000). STOA is based on similarity theory (Sedov, 1959) of blast waves, modified by the piston-driving concept, that emanate from point explosions (Dryer, 1974). In this model, the initial explosion (solar event) drives a shock.

The shock is assumed to be initially driven at a constant speed, Vs, for a specified length of time that is determined by the length of the GOES X-ray duration as a proxy (Smith et al., 2000). The shock is then allowed to decelerate as a blast wave (where the shock wave's speed, Vs ~ $R^{-1/2}$,and R is the heliocentric radius) as it expands outwards from the sun. The magnitude of the total energy conversion process determines the solid angle of quasi-spherical shock propagation, and how far the shock would propagate as it "rides over" a uniform background solar wind. It is assumed that the fastest part of the shock is nearly coincident with the radius vector from the center of the Sun through the flare site. The flanks of the shock would first decay via viscous and ohmic dissipation to an MHD wave [Jeffrey and Taniuti, 1964]; the fastest part would also eventually decay to an MHD wave.

The shock speed directly above the flare is usually determined from the observed metric type II radio frequency drift rate using an assumed coronal density model. However, none of the events of the new solar cycle, as of this writing, have been associated with metric type II bursts. In this case, the event was reported as a CME with corresponding plane-of-sky speeds. As a part of the forecasting program carried out on more than 675 events during the last solar cycle 23 [Fry et al., 2003; Smith et al., 2000; McKenna-Lawlor et al., 2006], it was found that the initial input shock velocity (from a solar flare's launch site near central meridian and in the absence of an observed metric radio Type II drift) was taken to be approximately twice the observed halo CME's plane-of-sky speed..

Based on the empirical studies of Lepping and Chao [1976], STOA uses a cosine function to account for longitudinal dependence of the shock geometry in the ecliptic plane. The shock speed is assumed to decrease from the maximum in the direction of the flare via this cosine function, to give a nonspherical shape in longitude. This spatially dependent shock speed is taken to be constant during the piston-driven phase.

During the blast wave phase, the longitudinal cosine shape is maintained. A relatively small energy output (probably $<10^{30}$ ergs or $<10^{23}$ joules) would result in the shock's decaying to an MHD wave prior to it reaching 1 AU. This decay would initially start at the flanks. STOA allows for a radially variable background solar wind, which is uniform in solar longitude. This is estimated from the solar wind velocity, V_{sw}, measured at L1 at the time of the flare. V_{sw} is used to determine the radially varying background solar wind speed through which the shock propagates, and thereby, the decay of the shock. No interplanetary structures such as stream–stream interactions are considered. Required observational data are as follows: the flare's solar longitude; the start time of the metric type II radio drift (essentially the peak time of the soft X-ray flux); the proxy piston-driving time duration to half-maximum; and V_{sw}. This last input provides a Parker-type radial and ecliptic plane speed profile that is assumed to be fixed until the shock arrives at L1.

The Fearless Forecast ensemble of models (Fry et al., 2003) was set up to accept the same input. This ensemble included STOA and three other models. Only STOA is included here because similar root mean squares (about $\pm$12 hr) were achieved as differences between predictions and "hits". For the event on 8 April, 2010, the input quantities for STOA were:

Start date	8 April 2010
Start time	03:25
Latitude	25^o North
Longitude	16^o East
Shock Velocity	600 kms^{-1}
Piston driving time	3 hours
Solar Wind Velocity	400 kms^{-1}

The start date and time correspond to the GOES event peak. Latitude and longitude refer to the location of the event in HEEQ solar coordinates. The shock velocity refers to the initial velocity of the shock, assumed (in the absence of a ground-based radio metric type II radio drift in the present case) to be twice that of the CME. The piston-driving time is measured from the width of the X-ray pulse at the linear half-width of the logarithmic scale of the NOAA GOES X-ray monitor. The solar wind velocity, V_{sw}, refers to the speed of the background solar wind measured at L1 at the time of the flare.

The STOA model physical output quantities are 1) shock arrival time at any point in the ecliptic plane (chosen to be Earth in this case), 2) estimate of the shock's Alfvén Mach number so that, when less than 1.0, it is implied that the shock has decayed to an MHD wave, and 3) total transit time from the low corona to Earth. The predictions output from this model were;

Mach 2.2 shock will reach Earth	11 April 2010 00:56
Total propagation time	69h 31m

There is no distinction, as in the Enlil model, between Earth and L1; both are the same grid point within the resolution of the model.

Assessing the accuracy of each forecast by comparison with in-situ data

Using the in-situ data described in the introduction, it is possible to compare the predictions made by each of the techniques listed above. Table II summarizes the accuracy of each of the predictions. Of the five techniques that are outlined in this paper, four used coronagraph images from either STEREO or SOHO to characterize the speed and direction of the CME while one used images from the wide-field HI cameras onboard STEREO. The exact feature associated with the CME also varies between techniques. Enhancements in electron density are tracked by their scattering of sunlight in the STEREO and SOHO images while the STOA technique predicts the arrival of the shock front. The ACE and WIND data reveal that, for this event at least, the leading edge of the density enhancement occurs at approximately the same time as the passage of the shock, so the arrival times of these two features can be considered to be the same.

Although some of the predictions in this comparison were more accurate than others, none predict the arrival time exactly. It is clear that to improve predictions further, either the influence of the ambient solar wind in accelerating the CME beyond the coronagraphs' field of view must be better characterized or the spatial and temporal resolution of measurements made with the HI cameras must be increased to provide a more accurate estimate of the CME speed in a region where the CME is likely to be undergoing little or no acceleration.

Conclusions

While this study focuses on a single event, there are two conclusions that can be drawn from this example. The most accurate prediction used STEREO coronagraph data to ascertain the speed and direction of the CME close to the Sun, then used a model of the ambient solar wind to account for any modulation of the CME speed as it propagated to 1 AU. Ascertaining the CME arrival time from HI measurements should, in principle, overcome the need to model such acceleration since the measurements are made at sufficiently large distances that the majority of this acceleration will have occurred. However the reduced temporal/spatial resolution of beacon mode data reduces the accuracy of this technique. When the science data from HI were subsequently used to estimate the arrival time of the ICME at Earth, the estimate was much closer to the arrival according to the in-situ data.

To put the conclusions drawn from this single event in context, more events need to be studied in this way, covering a range of CME speeds and solar wind conditions. To achieve this, predictions need to be made ahead of time and made available in a public forum, such as the STEREO Space Weather website, so that they are demonstrably unbiased by the availability of post-event information and analysis. . Other techniques, notably the Hakamada-Akasofu-Fry kinematical model (HAFv.2), are also used in real time (Fry et al., 2001, 2003; McKenna-Lawlor et al., 2006) to predict the shock arrival; however, this model does not include explicit consideration of the CME. Additional techniques, such as Tappin and Howard (2009) and Howard and Tappin (2010), which have been used for CME reconstruction, remain untested in a real-time forecasting environment.

Some advantage may be gained by combining some of the techniques listed within this paper. We show, for example, that it is possible to use the trajectory of the CME estimated from coronagraph data to constrain the HI measurements and produce a time/height profile in which any acceleration could be measured. For the 8 April CME, the CME and solar wind speeds were sufficiently close that no significant acceleration was detected in the HI data when combining these techniques. It would be interesting to repeat this analysis for a much faster CME.

There are many papers in the literature that reconstruct the sequence of events for individual CMEs in great detail. These studies invariably enjoy the luxury of using high-resolution science data drawn from many sources but after the fact. The challenge with true space-weather forecasting is to reconstruct events as they are happening, using data sets that are far less complete. It is important for the research community to realize that space weather forecasting tools must work with near-real time data; such data is usually compressed and/or binned and may have significant gaps in data coverage. Earth-orbiting solar imagers do not suffer from such limited telemetry rates as the more distant probes such as STEREO but because of their proximity to Earth do not provide the side-on view of the Sun-Earth line necessary to determine the true velocity of a solar transient. The relative merits of each of these systems will need to be considered when planning future operational space-weather missions.

Acknowledgements

The authors would like to thank N. Ness at the Bartol Research Institute for supplying the ACE Magnetic field data and D. J. MComas at the Southwest Research Institute for the ACE/SWEPAM data. Both datasets were accessed from the CDAWeb interface supported by the Goddard Space Flight Center via their website at http://cdaweb.gsfc.nasa.gov. DW was supported by U.S. Navy contract N00173-10-1-G-001. CJF was supported by NASA grant NNX10AQ29G. CADK was supported by NASA grant NNX09AJ84G.

References

Arge, C. N., Luhmann, J. G., Odstrcil, D., Schrijver, C. J., Li, Y., Stream structure and coronal sources of the solar wind during the Math 12th, 1997 CME, J. Atmos. Sol. Terr. Phys., 66, 1295-1309, 2004.

Biesecker, D. A., Webb, D. F., Cyr, O. C. S., STEREO space weather and the Space Weather Beacon, Space Sci. Rev., 136, 45-65, 2008.

Brueckner, G. E., Howard, R. A., Koomen, M. J., Korendyke, C. M., Michels, D. J., Moses, J. D., Socker, D. G., Dere, K. P., Lamy, P. L., Llebaria, A., Bout, M. V., Schwenn, R., Simnett, G. M., Bedford, D. K., Eyles, C. J.,., The Large Angle Spectroscopic Coronagraph (LASCO), Sol. Phys., 162, 357-402, 1995.

Davies, J. A., Harrison, R. A., Rouillard, A. P., Sheeley, N. R., Perry, C. H., Bewsher, D. Davis, C. J., Eyles, C. J., Crothers, S. R., Brown, D. S., A synoptic view of solar transient evolution in the inner heliosphere using the Heliospheric Imagers on STEREO, Geophys. Res. Lett., 36, 2009.

Davis, C. J., Davies, J. A., Lockwood, M., Rouillard, A. P., Eyles, C. J., Harrison, R. A., Stereoscopic imaging of an Earth-impacting solar coronal mass ejection: A major milestone for the STEREO mission, Geophys. Res. Lett., 36, 2009.

Davis, C. J., Kennedy, J, Davies, J. A., Assessing the accuracy of CME speed and trajectory estimates from STEREO observations through a comparison of independent methods, Sol. Phys., 263, 209-222, 2010.

de Koning C. A., Pizzo, V. J., Biesecker, D. A., Geometric localization of CMEs in 3D space using STEREO beacon data: First results, Sol. Phys., 256, 2009.

de Koning, C. A., Pizzo, V. J., Polarimetric Localization: A New Tool for Calculating the CME Speed and Direction of Propagation in Near-Real Time, Space Weather, in press, 2010.

Dryer, M., Interplanetery shock waves generated by solar flares, J. Geophys. Res., 15, 403-468, 1974.

Dryer, M., and S.F. Smart, Dynamical models of coronal transients and interplanetery disturbances, Adv. Space Res., 4, 7, 291-301, 1984.

Eichstedt, J., Thompson, W. T., Cyr, O. C. S., STEREO ground segment, science operations and data archive, Space Sci. Rev., 136, 605-626, 2008.

Eyles, C. J., Harrison, R. A., Davis, C. J., Waltham, N. R., Shaughnessy, B. M., Mapson-Menard, H. C. A., Bewsher, D., Crothers, S. R., Davies, J. A., Simnett, G. M., Howard, R. A., Moses, J. D., Newark, J. S., Socker, D. G., Halain, J. P., Defise, J. M., Mazy, E., Rochus, P., The Heliospheric Imagers Onboard the STEREO Mission, Solar Physics, 254, 387-445, 2009.

Farrugia, C. J., N. V. Erkaev, H. K. Biernat, and L. F. Burlaga, Anomalous magnetosheath properties during Earth passage of an interplanetary magnetic cloud, J. Geophys. Res., 100, 19, 245, 1995.

Fleck, B., Domingo, V., and Poland, A., The SOHO Mission, Kluwer Academic Publishers, 1995.

Fry, C. D., W. Sun, C. S. Deehr, M. Dryer, Z. Smith, S. I. Akasofu, M. Tokumaru, M. Kojima, Improvements to the HAF solar wind model for space weather predictions, J. Geophys. Res., 106, 20985-21001, 2001.

Fry, C.D., M. Dryer, Z.K. Smith, W. Sun, C. Deehr, and S. Akasofu, Forecasting solar wind structures and shock arrival times using an ensemble of models, J. Geophys. Res., 108 (A2), 2003.

Gopalswamy, N., A. Lara, R. P. Lepping, M. L. Kaiser, D. Berdichevsky and O. C. St. Cyr, Interplanetary acceleration of coronal mass ejections, Geophys. Res. Lett, 27, 145-148, 2000.

Gosling, J. T., V. Pizzo, and S. J. Bame, Anomalously low proton temperatures in the solar wind following interplanetary shock waves: Evidence for magnetic bottles?, J . Geophys. Res., 78, 2001, 1973

Gosling, J. T., and McComas, Field line draping about fast coronal mass ejecta: A source of strong out-of-the-ecliptic magnetic fields, Geophys. Res. Lett., 14, 4, 355-358, 1987.

Howard, R. A., Moses, J. D., Vourlidas, A., et al., Sun Earth Connection Coronal and Heliospheric Investigation (SECCHI), Space Sci. Rev., 136, 67-115, 2008.

Howard, T. A., and S. J. Tappin, Application of a new phenomenological coronal mass ejection model to space weather forecasting, Space Weather, 8, S07004, 2010.

Jeffrey, A., and T. Taniuti, Non-Linear Wave Propagation With Applications to Physics and Magnetohydrodynamics, Academic Press, San Diego, 1964.

Jones, R. A., A. R. Breen, R. A. Fallows, A. Canals, M. M. Bisi and G. Lawrence, Interaction between coronal mass ejections and the solar wind, J. Geophys. Res., 112, A08107, 2007.

Lavraud, B., and J. E. Borovsky, Altered solar wind-magnetosphere interaction at low Mach numbers: Coronal mass ejections, J.Geophys. Res., 113, A00B08, doi: 10.1029/2008JA013192, 2008.

Lepping, R., and J.-K. Chao, A shock surface geometry: The 15-16 February 1967 event, J. Geophys. Res., 81, 60-64, 1976.

Lepping, R. P., Acuna, M. H., Burlaga, L. F., Farrel, W. M., Slavein, J. A., Schatten, K. H., Mariani, F., Ness, N. F., Neubauer, F. M., Whang, Y. C., Byrnes, J. B., Kennon, R. S., Panetta, P. V., Scheifele, J., Worley, E. M., : The Wind Magnetic Field Investigation, Space Sci. Rev., 71, 207-229, 1995.

Lopez, R. E., Solar cycle invariance in solar wind proton temperature relationships, J. Geophys. Res., 92, 11, 187, 1987.

McComas, D. J., Bame, S. J., Barker, P., Feldman, W. C., Phillips, J. L., Riley, P. Griffee, J. W., Solar Wind Electron Proton Alpha Monitor (SWEPAM) for the Advanced Composition Explorer, 86, 563-612, 1998.

McKenna-Lawlor, S. M. P., M. Dryer, M. D. Kartalev, Z. Smith, C. D. Fry, W. Sun, C. S. Deehr, K. Kecskemety, and K. Kudela, Near real-time predictions of the arrival at Earth of flare-related shocks during Solar Cycle 23, J. Geophys. Res., 111, A11103, doi:10.1029/2005JA011162, 2006.

Moran, T. G. & Davila, J. M., Three-dimensional polarmetric imaging of coronal mass ejections, Science, 305, 66, 2004.

Odstrcil, D., Pizzo, V. J., Three-dimensional propagation of coronal mass ejections (CMEs) in a structured solar wind flow 1. CME launched within the streamer, J. Geophys. Res., 104, 483-492, 1999a.

Odstrcil, D., Pizzo, V. J., Distortion of the interplanetary magnetic field by three-dimensional propagation of coronal mass ejections in a structured solar wind, J. Geophys. Res., 104, 28225-28239, 1999b.

Ogilvie, K. W., J. D. Scudder, and M. Sugiura, Electron energy flux in the solar wind, J. Geophys. Res., 76, 8165, 1971.

Ogilvie, K. W. and Parks, G. K., First results from the WIND spacecraft: An Introduction, Geophys. Res. Lett., 23, 1179-1181, 1996.

Pilipp, W. G., H. Miggenrieder, M. D. Montgomery, K.-H. Mühlhäuser, H. Rosenbauer, and R. Schwenn Unusual electron distribution functions in the solar wind derved from the Helios plasma experiment: Double-strahl distributions and distributions with an extremely anisotropic core, J. Geophys. Res., 92(A2), 1093-1101, 1987.

Pizzo, V. J., Biesecker, D. A., Geometric localization of STEREO CMEs, Geophys. Res. Lett., 31, L21802, 2004.

Richardson, I., and H. Cane Regions of Abnormally Low Proton Temperature in the Solar Wind (1965-1991) and their Association with Ejecta, J. Geophys. Res., 100(A12), 23397-23412, 1995.

Rouillard, A. P., Davies, J. A., Forsyth, R. J., Rees, A., Davis, C. J., Harrison, R. A., Lockwood, M., Bewsher, D., Crothers, S. R., Eyles, C. J., Hapgood, M., Perry, C. H., First imaging of corotating interaction regions using the STEREO spacecraft, Geophys. Res. Lett., 35, L10110, 2008.

Russell, C. et al., The STEREO mission, Springer, 2008.

St. Cyr, C., The last word: The definition of Halo Coronal Mass Ejections, Eos, Trans. AGU, 86, 30, 281-282, doi 10.1029/2005EO300005, 2005

Sedov, L.I., *Similarity and Dimensional Methods in Mechanics*, Chapters 4 & 5, Academic Press, San Diego, 1959.

Sheeley, N. R., Walters, J. H., Wang, Y. M., Howard, R. A, Continuous tracking of coronal outflows: Two kinds of coronal mass ejections, J. Geophys. Res., 104, 24739-24767, 1999.

Sheeley, N. R., Herbst, A. D., Palatchi, C. A., Wang, Y. M., Howard, R. A., Moses, J. D., Vourlidas, A., Newmark, J. S., Socker, D. G., Plunkett, S. P., Korendyke, C. M., Burlaga, L. F., Davilla, J. M., Thompson, W. T., St Cyr, O. C., Harrison, R. A., Davis, C. J., Eyles, C. J., Halain, J. P., Wang, D., Rich, N. B., Battams, K., Esfandiari, E., Stenborg, G., Heliospheric Images of the solar wind at Earth, Astrophys. J., 675, 853-862, 2008.

Smart, D.F., and M.A. Shea, A simplified model for timing the arrival of solar -flare-initiated shocks, J. Geophys. Res., 90, 183-190, 1985.

Smith, Z., M. Dryer, and W. Murtagh, Performance of interplanetary shock prediction models: STOA and ISPM, J. Atmos. Solar-Terr. Phys., 62, 1265-1274, 2000.

Stone, E. C., Burlaga, L. F., Cummings, A. C., Feldman, W. C., Frain, W. E., Geiss, J., Gloeckler, G., Gold, R. E., Hovestadt, D., Krimigis, S. M., Mason, G. M., McComas, D., Mewaldt, R. A., Simpson, J. A., Vonrosenvinge, T. T., Wiedenbeck, M. E., The Advanced Composition Explorer, Space Sci. Rev., 86, 1-22, 1998.

Tappin, S. J., and T. A. Howard, Interplanetary Coronal Mass Ejections Observed in the Heliosphere: 2. Model and Data Comparison, Space Sci. Rev., 147, 55-87, 2009.

Thernisien, A., Vourlidas, A., Howard, R. A., Forward Modeling of Coronal Mass Ejections Using STEREO/SECCHI Data, Solar Phys., 256, 111-130, 2009.

Wing, T. D., GONG magnetic field images, SOHO/6GONG 98 Workshop on Structure and Dynamics of the Interior of the Sun and Sun-like Stars. Volume 418m, 625-626, 1998.

Xie, H., Ofman, L., Lawrence, G., Cone model for halo CMEs: Application to space weather forecasting, J. Geophys. Res., 109, A3, A03109, 2004.

Yurchyshyn, V., Wang, H., Goode, P.R., Deng, Y., Orientation of the Magnetic Fields in Interplanetary Flux Ropes and Solar Filaments, The Astrophysical Journal, 563, 381-388, 2001.

Yurychyshn, V., Relationship between EIT Posteruption Arcades, Coronal Mass Ejections, the Coronal Neutral Line, and Magnetic Clouds, The Astrophysical Journal Letters, 675, L49-L52, 2008.

Zhao, X. P., and Hoeksema, J. T., Central axial field direction in magnetic clouds and its relation to southward interplanetary magnetic field events and dependence on disappearing solar filaments, J. Geophys. Res., 103, 2077, 1998

Measured and predicted CME speeds and directions				
Technique	Speed measured in coronagraph data	Assumed solar wind speed (kms^{-1})	Predicted Speed at 1 AU (kms^{-1})	Predicted direction (HEE longitude, degrees)
COR2 (geometric localization)	469 ± 27	-	469 ± 27	2 ± 13 east
COR2 (polarisation STEREO-A)	473 ± 59	-	473 ± 59	11 ± 3 west
COR2 (polarisation STEREO-B)	545 ± 42	-	545 ± 42	15 ± 1 east
HI	-	-	417 ± 67	12 ± 17 east
Biesecker	424.9	ACE data	-	-
Enlil (SOHO/LASCO)	424.9	WSA model	-	-
Enlil (STEREO/COR2)	469 ± 27	WSA model	-	-
STOA	600 (shock)	400	-	-

Table I

The STOA input shock speed in the 2nd column, in the absence of a metric Type II observation and speed estimate, was assumed to be approximately twice the initial LASCO C3 measurement (286 km/s) of the halo CME at 06:18 on 8 April 2010 (see text).

Predicted ICME arrival times compared with in-situ measurements				
Technique	Predicted arrival at ACE	Predicted arrival at Earth	Difference from in-situ observation (hours)	Lead time of prediction (days)
COR2 (geometric localization)	17:40 UT ± 5 11 April 2010		+5.43	2.16
HI	01:13 UT ± 1.18 12 April 2010	02:13 UT ± 1.18 12 April 2010	+12.98	2.0
Biesecker	06:30 UT ± 8 11 April 2010	06:30 UT ± 8 11 April 2010	-5.73	1.6
Enlil (SOHO/LASCO)	21:00 UT 11 April 2010	21:00 UT 11 April 2010	+8.75	0.6
Enlil (STEREO/COR2)	09:00 UT 11 April 2010	09:00 UT 11 April 2010	-3.25	0.6
STOA	00:56 UT ± 12 11 April 2010	00:56 UT ± 12 11 April 2010	-12.25	1.5

Table II

Note: All predictions, except for STOA (Shock Time of Arrival) refer to the ICME which was observed at L1 at 12:14 UT on 11 April 2010.

Figure 1 (a) SOHO MDI magnetogram during the flare on 8 April at 03:15 UT (black negative polarity, white positive) with the estimated tilt angle of the active region neutral line to the solar equator (red). (b) The GONG potential field source surface model with the coronal neutral line (yellow) and the source region indicated. (c) SOHO LASCO C2 observations of the estimated tilt angle of the halo CME (green).

Figure 2 ACE observations during the passage of the ICME through the L1 point. From top to bottom these panels show; the three components of the Interplanetary Magnetic Field (IMF) in GSM coordinates, the total magnetic field strength, the solar wind bulk velocity, the proton number density and temperature. The passage of a shock is indicated by the dashed vertical line at 12:14 UT on 11 April 2010. The ensuing enhancement in solar wind density followed by an enhancement and rotation of the IMF reveals the passage of the ICME.

Figure 3 Plasma and magnetic field observations from the SWE and the MFI instruments on the Wind spacecraft for the time interval 12 UT, 10 April to 12 UT, 13 April showing the passage of the ICME past the WIND spacecraft at the L1 point. The data are at ~95 s temporal resolution. From top to bottom are plotted the proton number density, temperature, bulk speed, dynamic pressure, total field strength and components of the magnetic field in GSE coordinates, the proton beta (in red: the Alfvén Mach number) and the pressures (red: magnetic; blue: proton thermal; black: their sum). The red trace in panel 2 is the expected proton temperature for normal solar wind expansion.

Figure 4 The pitch angle distribution of suprathermal electrons centered on E = 193.4 eV during the ICME interval. The data are from the Wind SWE/electron instrument and are plotted at 12 s resolution. It is seen that the strahl electrons, which carry the heat flux from the Sun, are generally unidirectional. Electrons are flowing against the field (large pitch angle) until ~1 UT, 12 April (indicated by the arrow), and then are flowing along the field (small pitch angle). A period of isotropic flow is indicated by a horizontal line above the plot.

Figure 5 Beacon (a, b) and science data (c, d) images taken at similar times from the STEREO COR2 coronagraphs. It is apparent that the level of detail in the science images is much greater than in the beacon images but the overall extent of the CME observed in both science and beacon data is similar for this particular case.

Figure 6 The reconstructed CME projected onto the equatorial plane of the Sun on 8 April 2010 at 07:08 UT; Earth is toward the bottom of the plot. The scale size is indicated by the hash marks, which are shown every 1 Rsun; in addition, concentric circles are shown every 5 Rsun. The viewing latitudes and longitudes on the plots refer to the observers position in HCI coordinates. The red points indicate the CME location as derived from COR2-A percent polarisation measurements, the blue points indicate the CME location as derived from COR2-B percent polarisation measurements, and the green quadrilaterals indicate CME location as derived from geometric localization; superimposed on this stack are purple quadrilaterals showing the location of the leading-edge.

Figure 7 Beacon and science data images of the ICME from the STEREO Heliospheric Imagers. The presence of the ICME in each case is revealed by looking at the difference between consecutive images in a time sequence. In this format, density enhancements appear light while density depletions appear dark so a feature propagating across the image will be seen to have a light leading edge and a dark trailing edge. Panels a and b show lossily compressed and binned HI-1 images from the STEREO A and B spacecraft, respectively, while panels c and d show similar images obtained from the higher resolution science data from HI-1 on the STEREO A and B spacecraft, respectively. The difference in resolution between the beacon and science data streams is apparent with much more detailed structure visible in the science data.

Figure 8 "J-maps" constructed from STEREO HI beacon mode and science images. These are created by taking a strip through each image along the ecliptic (corresponding to the position angle of the Earth) and stacking them vertically with time. The result is a map of elongation versus time in which any outward propagating solar wind transient appears as a feature with a positive gradient. As these J-maps are constructed from difference images, such as those shown in figure 7, each feature appears with a light leading edge and a dark trailing edge. To estimate the speed and direction of the ICME from the J-maps, the leading edge of the feature was scaled by hand and the resulting time/elongation profiles were analysed to estimate speed and direction of the ICME density front. As for figure 7, panels a and b are the J-maps constructed from the HI-A and HI-B beacon data, respectively, while panels c and d are the J-maps constructed from the HI-A and HI-B science data for the same period. The data gaps in the HI-A beacon J-map (panel a) meant that for this event the speed and direction of the ICME were estimated from the HI-B beacon data. The extra detail apparent in the science data J-maps (panels c and d) enabled an improved estimate of the ICME arrival time to be obtained after the event. The horizontal line at elongations of 57^{o} and 55^{o} in panel c and d respectively is the Earth. The ICME can be seen to propagate out to these elongations in both HI-A and HI-B (the latter having a noisier background because of particle impacts on the instrument and the presence of the Milky Way).

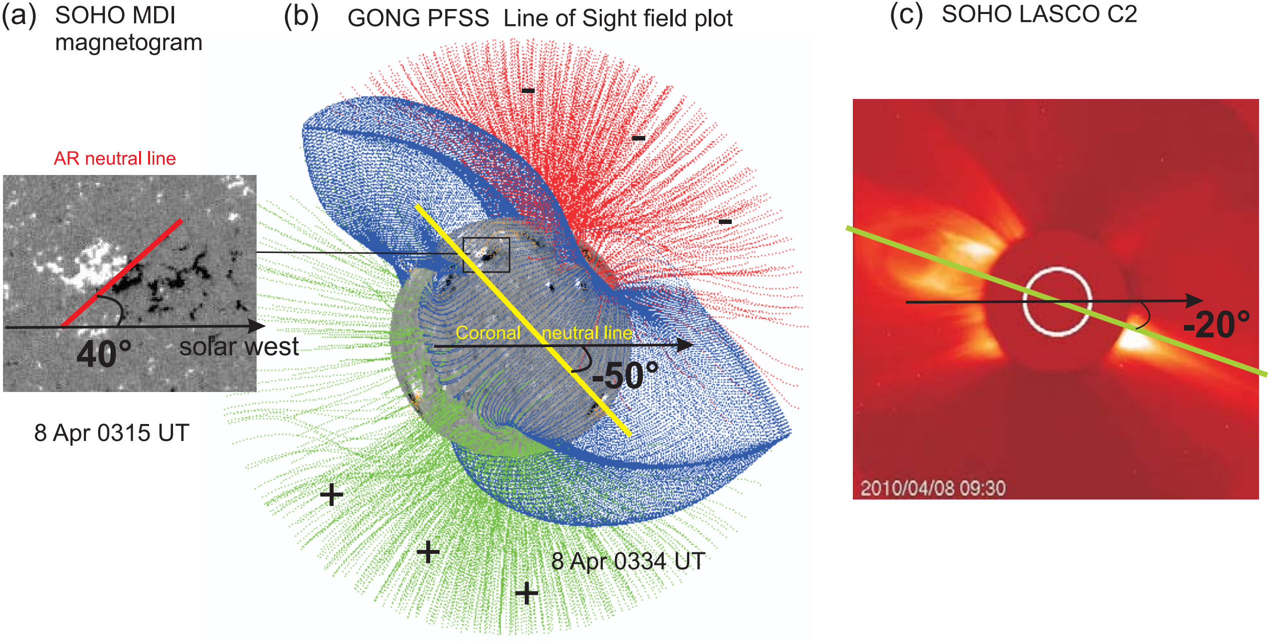
(a) SOHO MDI magnetogram
AR neutral line
40°
solar west
8 Apr 0315 UT
(b) GONG PFSS Line of Sight field plot
Coronal neutral line
-50°
8 Apr 0334 UT
(c) SOHO LASCO C2
-20°
2010/04/08 09:30

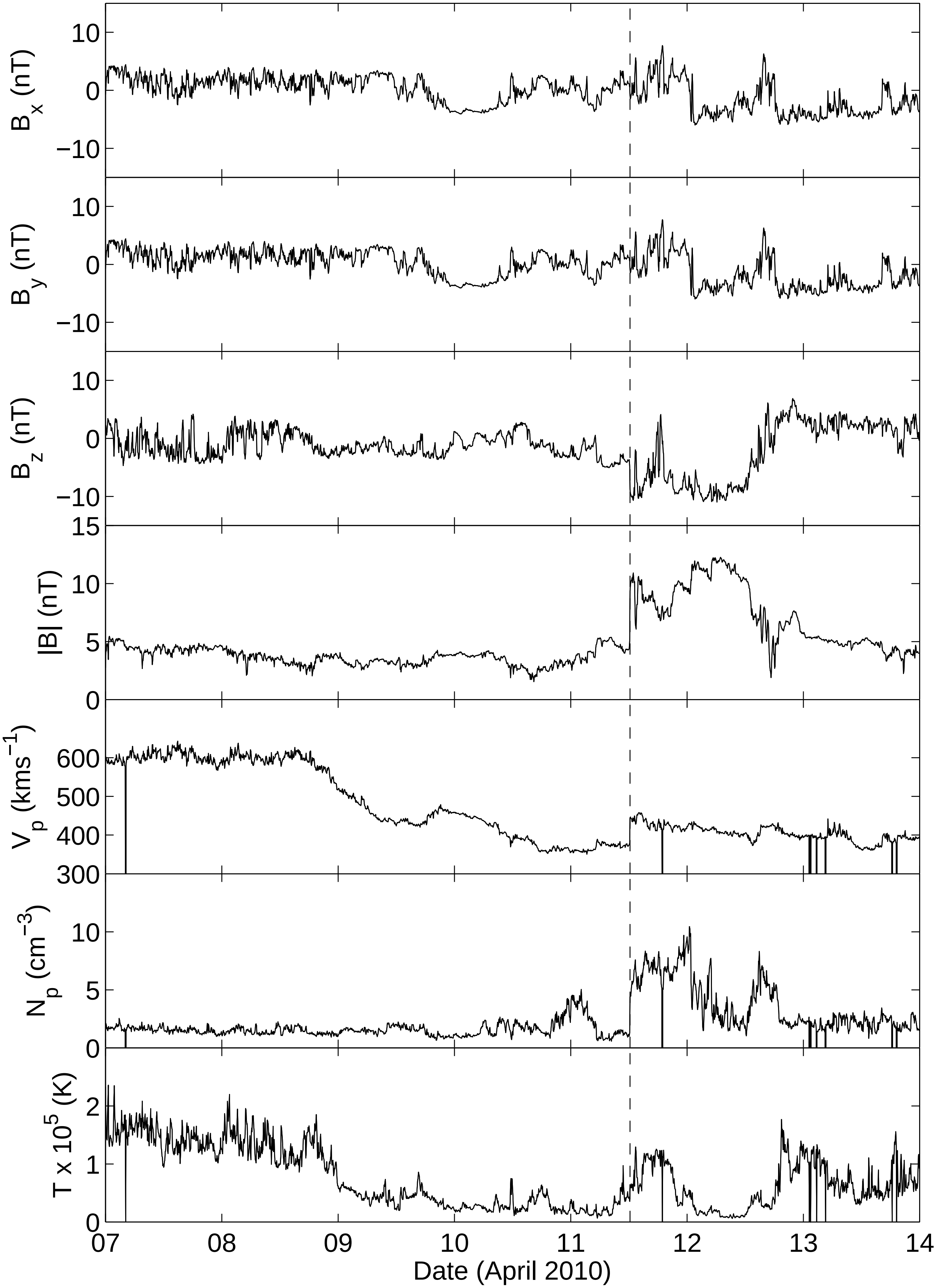

B_x (nT)
B_y (nT)
B_z (nT)
|B| (nT)
V_p (kms^{-1})
N_p (cm^{-3})
T x 10^5 (K)
Date (April 2010)

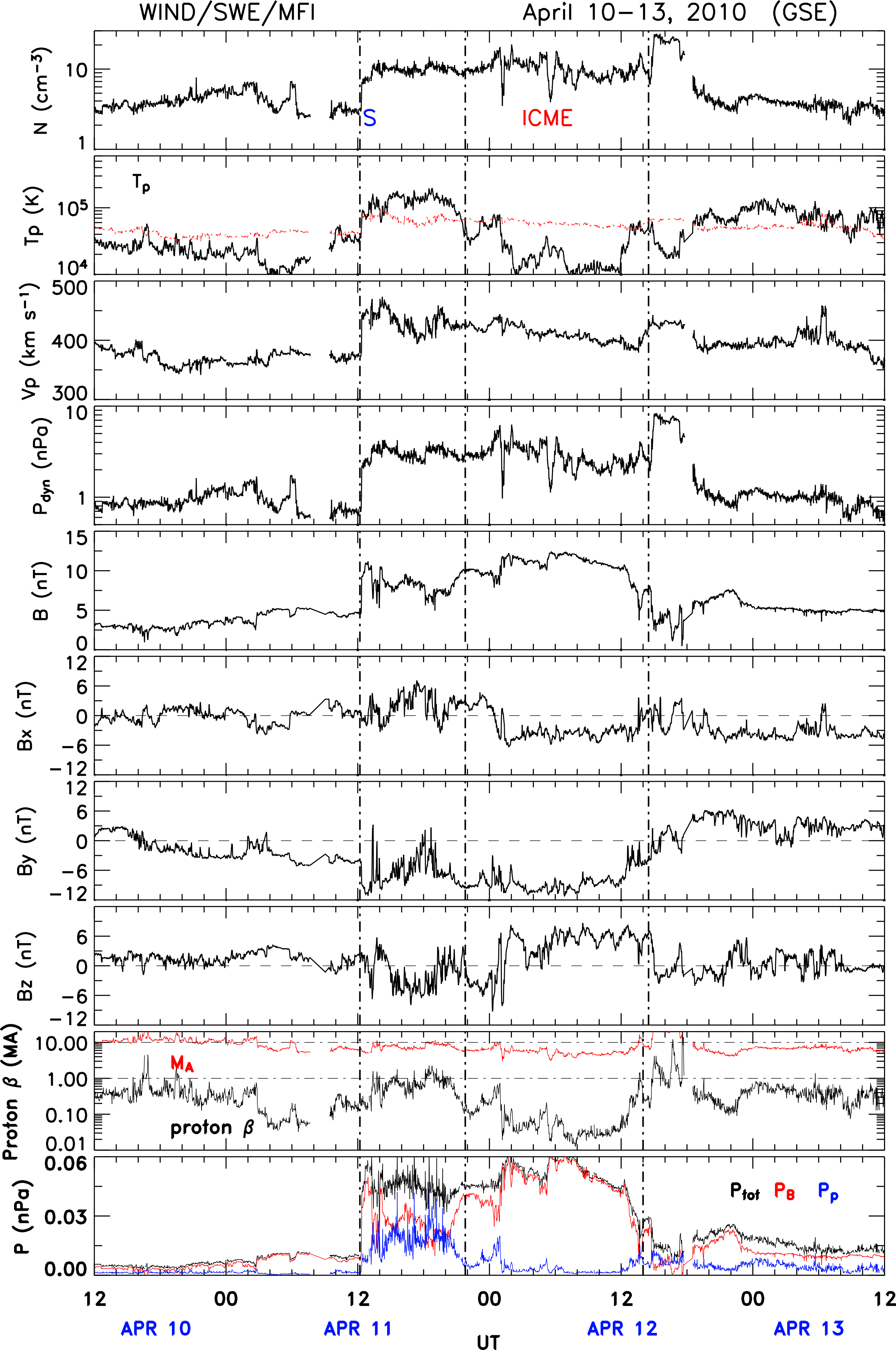

WIND/SWE/MFI
April 10−13, 2010 (GSE)
N (cm⁻³)
S
ICME
Tp
Tp (K)
Vp (km s⁻¹)
Pdyn (nPa)
B (nT)
Bx (nT)
By (nT)
Bz (nT)
Proton β (MA)
MA
proton β
P (nPa)
Ptot PB Pp
12
00
12
00
12
00
12
APR 10
APR 11
APR 12
APR 13
UT

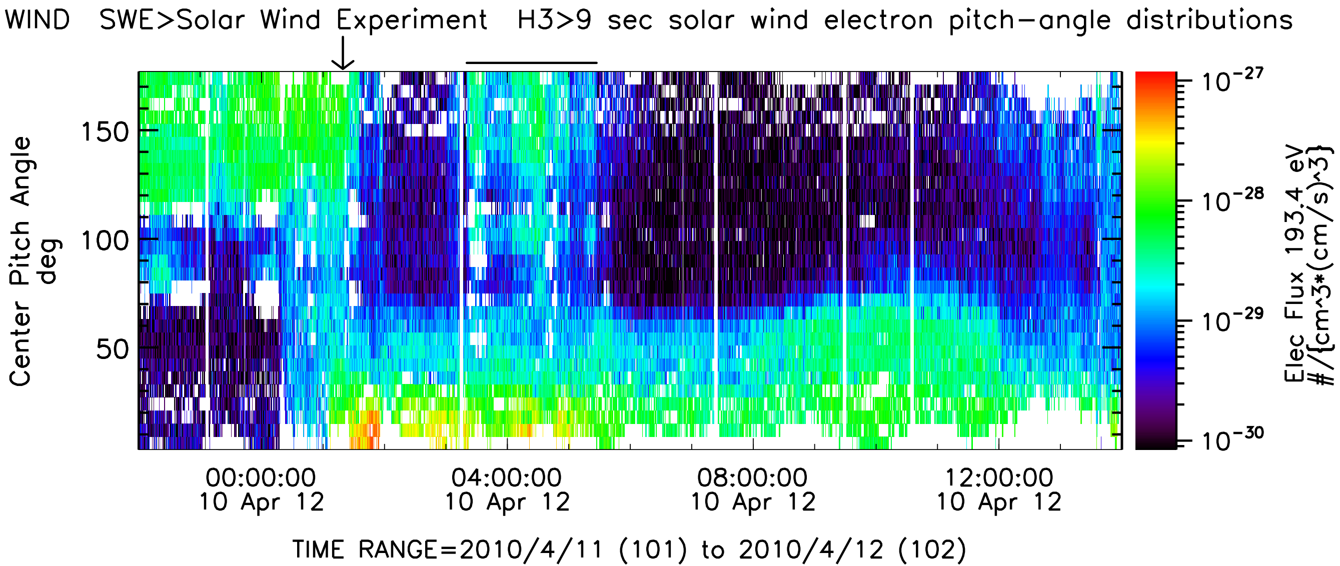
WIND SWE>Solar Wind Experiment H3>9 sec solar wind electron pitch-angle distributions
Center Pitch Angle deg
150
100
50
00:00:00 10 Apr 12
04:00:00 10 Apr 12
08:00:00 10 Apr 12
12:00:00 10 Apr 12
TIME RANGE=2010/4/11 (101) to 2010/4/12 (102)
Elec Flux 193.4 eV #/{cm^3*(cm/s)^3}
10^-27
10^-28
10^-29
10^-30

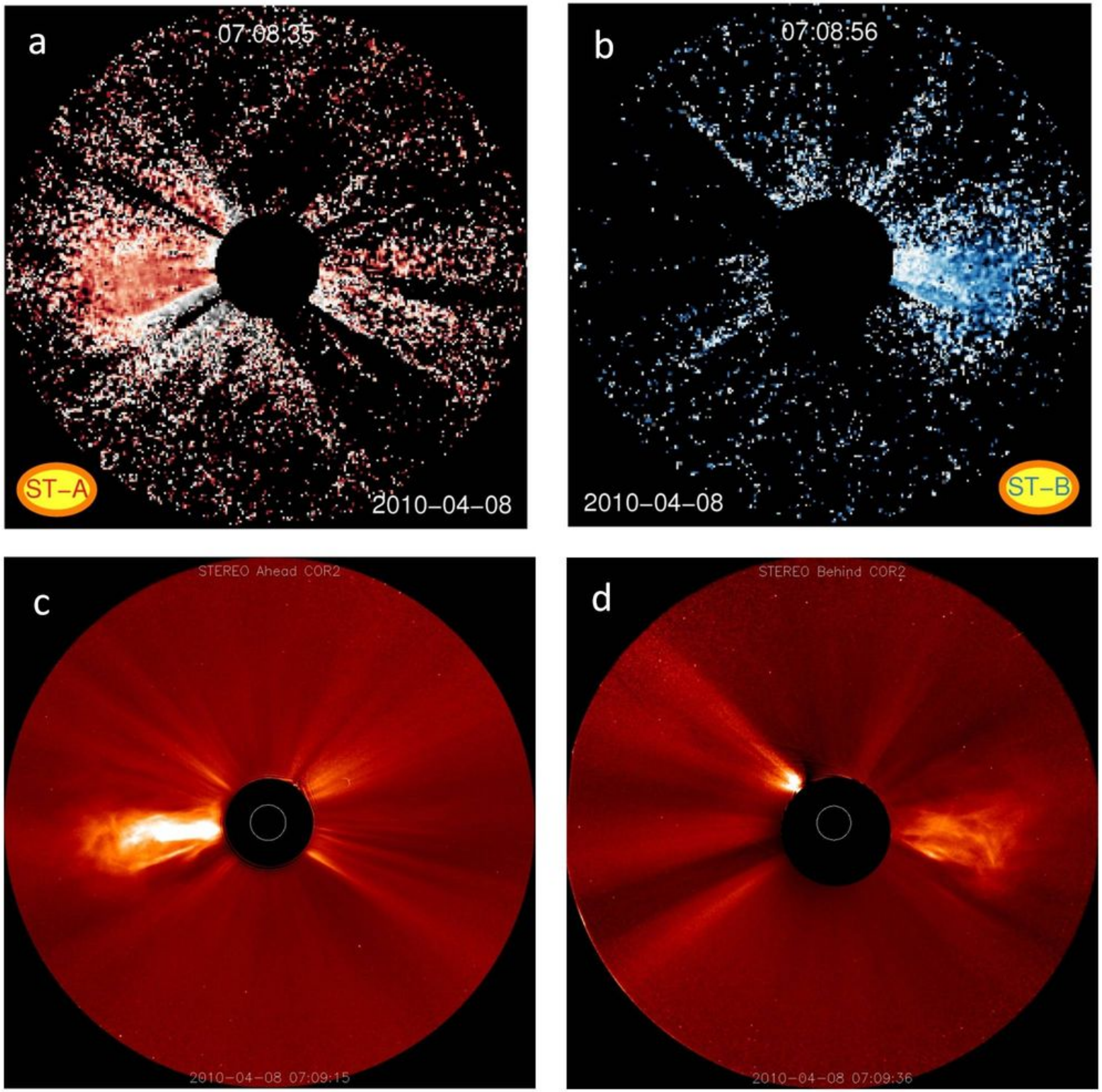
a
07:08:35
ST–A
2010-04-08
b
07:08:56
2010-04-08
ST–B
c
STEREO Ahead COR2
2010-04-08 07:09:15
d
STEREO Behind COR2
2010-04-08 07:09:36

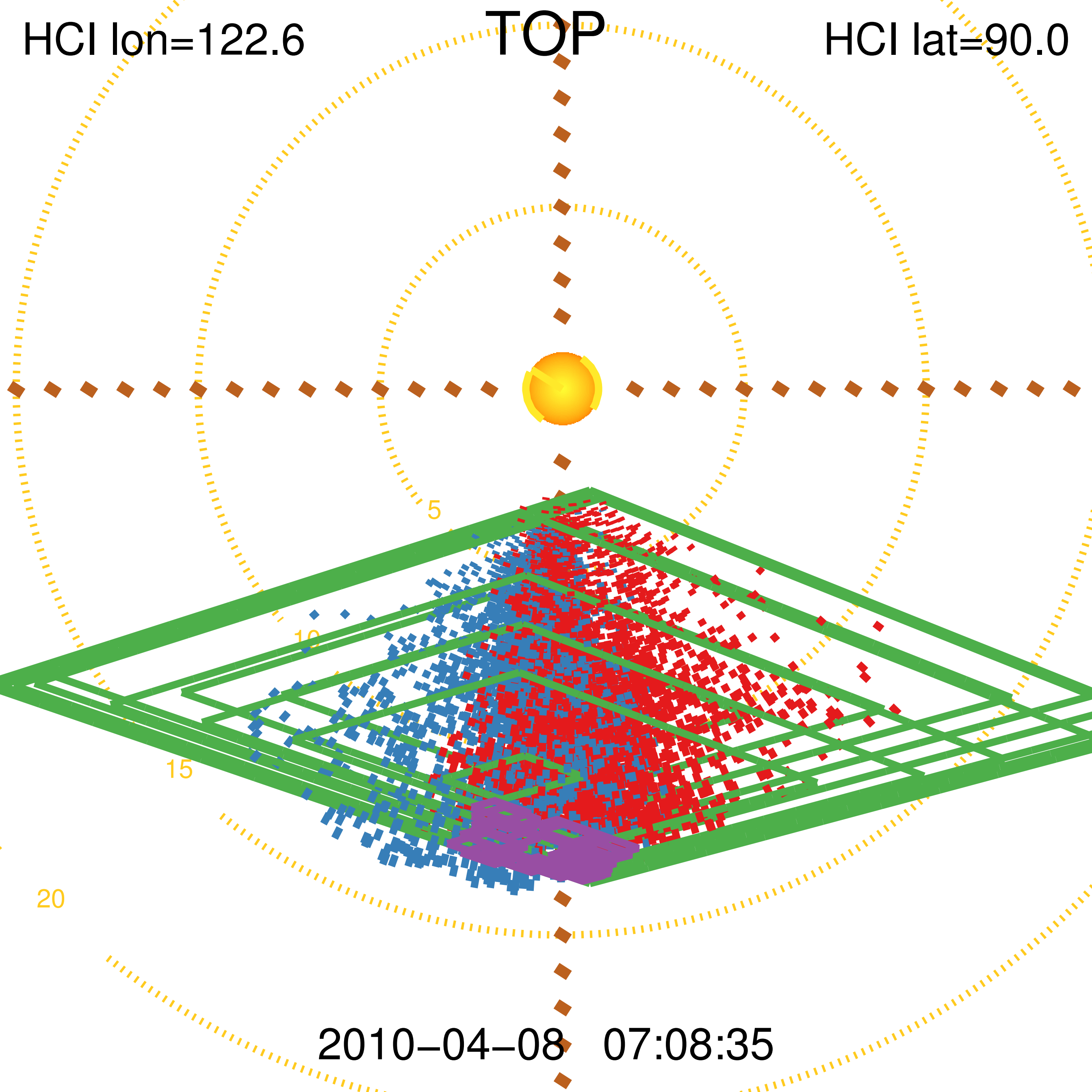

HCI lon=122.6
TOP
HCI lat=90.0
5
10
15
20
2010−04−08 07:08:35

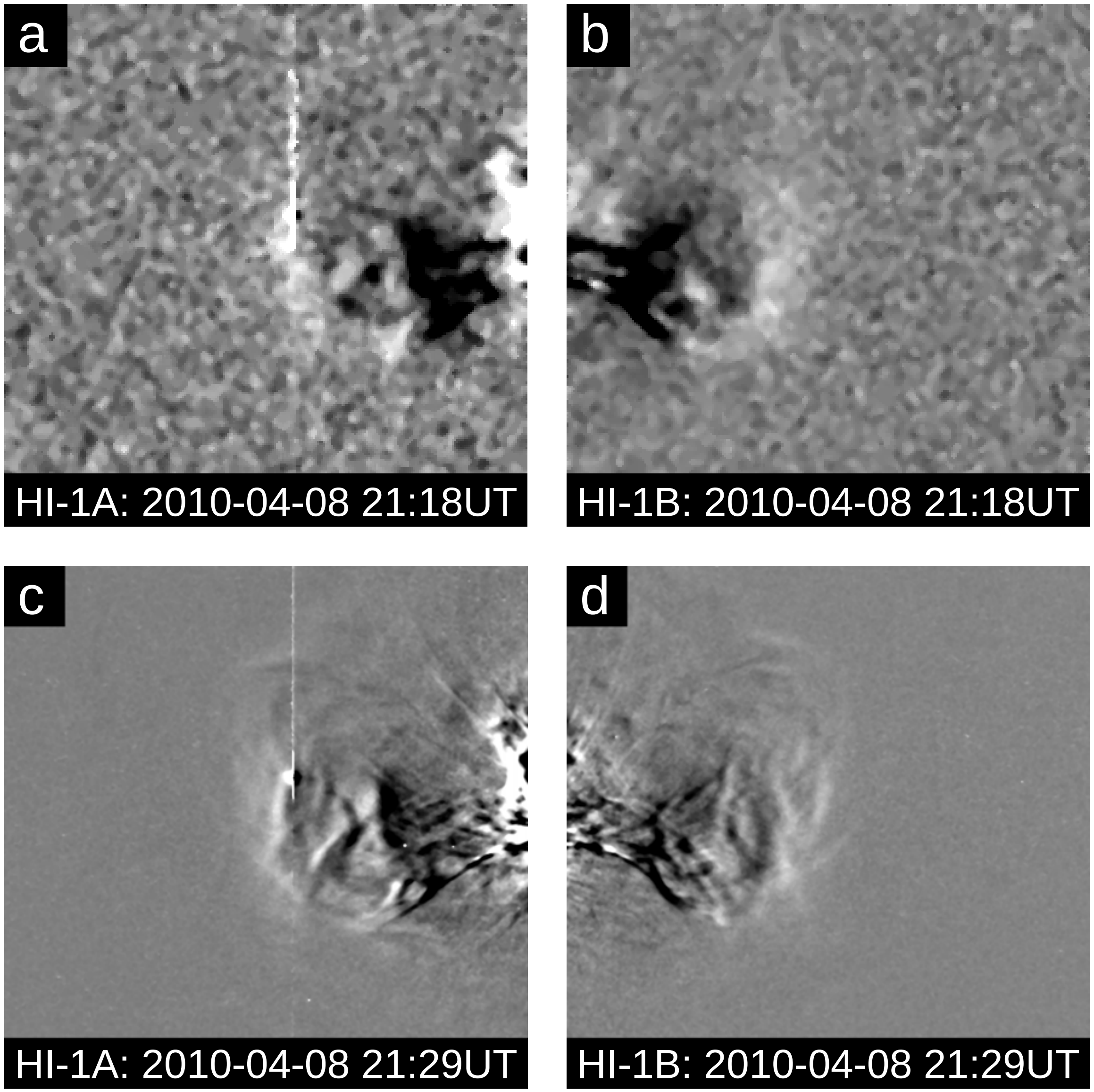
a
HI-1A: 2010-04-08 21:18UT
b
HI-1B: 2010-04-08 21:18UT
c
HI-1A: 2010-04-08 21:29UT
d
HI-1B: 2010-04-08 21:29UT

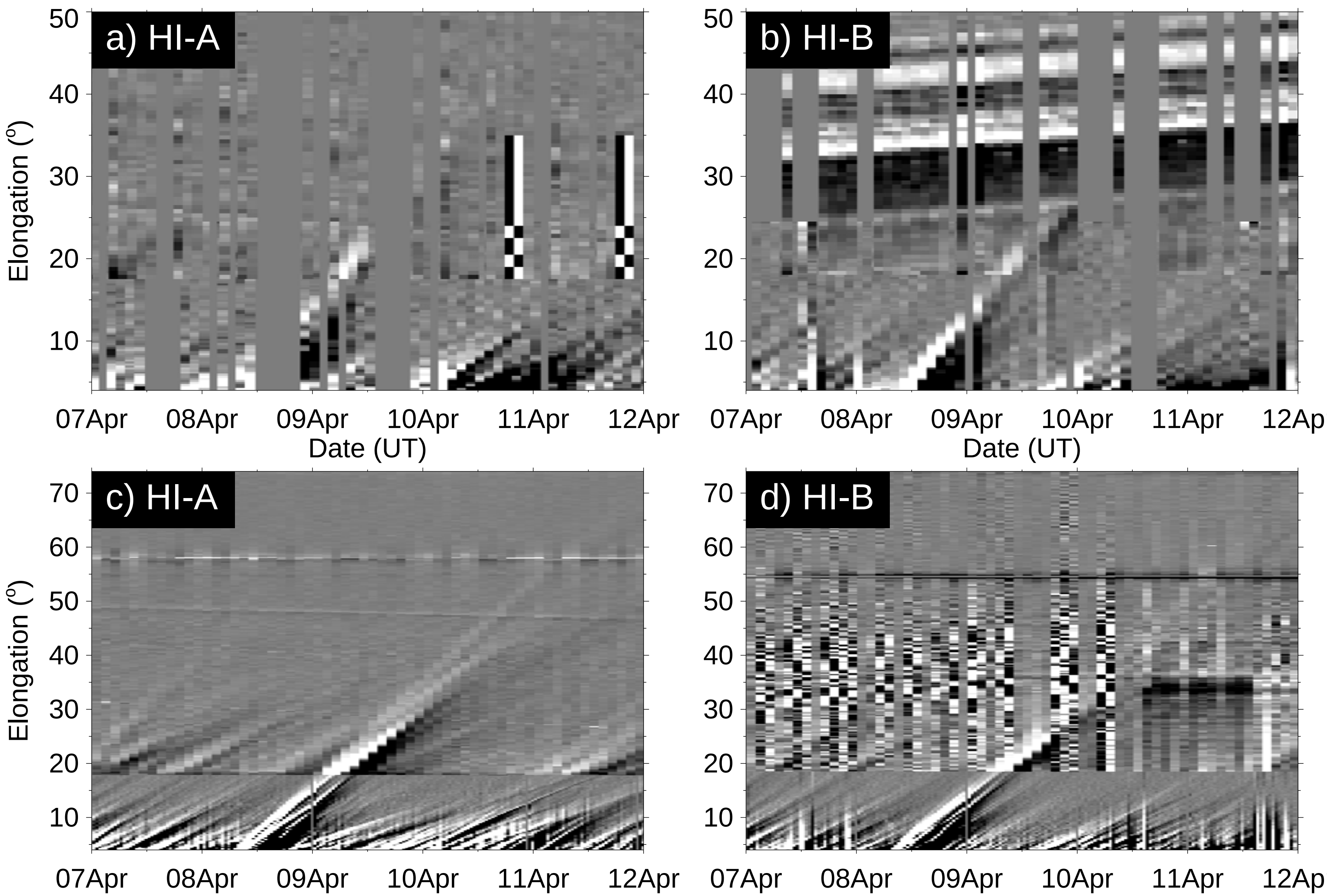

a) HI-A
b) HI-B
c) HI-A
d) HI-B
Elongation (°)
Date (UT)
07Apr
08Apr
09Apr
10Apr
11Apr
12Apr
10
20
30
40
50
60
70